Title
Prediction of Rotorcraft Broadband Trailing-Edge Noise and Parameter Sensitivity Study

Journal
Journal of the American Helicopter Society, 65(4)

ISSN
0002-8711

Authors
Li, Sicheng
Lee, Seongkyu

Publication Date
2020-10-01

DOI
10.4050/jahs.65.042006

Prediction of Rotorcraft Broadband Trailing-Edge Noise and Parameter Sensitivity Study

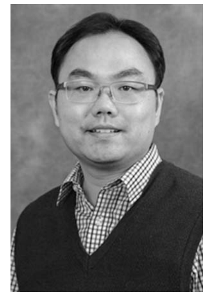

Sicheng (Kevin) Li*
Ph.D. Student

Seongkyu Lee
Associate Professor

Department of Mechanical and Aerospace Engineering, University of California, Davis, CA

This paper investigates the effects of rotorcraft design and operating parameters on trailing-edge noise. A rotor trailing-edge noise prediction method is first developed where the aerodynamics and the turbulence wall pressure spectrum near the trailing edge on airfoils are predicted by a combination of the standard blade element momentum theory , a viscous boundary-layer panel method, and a recently developed empirical wall pressure spectrum model. The coordinate transformations are combined with the Amiet model to predict far-field noise. Compared to experimental data, the validation of this method demonstrates its advantages and validity for airfoil and rotorcraft broadband noise predictions. Then, this method is used to study the effects of rotorcraft design and operating parameters on rotor trailing-edge noise. It is found that helicopter broadband noise scales with the 4.5th to 5.0th power of the tip Mach number in which the range is determined by the typical helicopter collective pitch angle in operation. Detailed trend analyses of noise levels as a function of frequency are presented in terms of the collective pitch angle, twist angle, rotor solidity, rotor radius, disk loading, and number of blades. It is found that the collective pitch angle, twist angle, and chord length make noticeable impacts on low- and midfrequency noise. Finally, a semianalytic model is presented to predict the directivity and geometric attenuation of rotor trailing-edge noise.

Nomenclature

C_f	skin friction coefficient
C_T	thrust coefficient
c	chord length, m
c_o	speed of sound, m/s
D	rotor diameter, m
D_ϕ	directivity term
d	rotor diameter, m
dp/dx	pressure gradient, Pa/m
E^*	complex conjugate of a Fresnel integral
f	frequency, Hz
k_x	chordwise wavenumber, 1/m
L	effective lift function, N/m
l_r	spanwise turbulence lengthscale, m
M	freestream Mach number
M_r	rotational Mach number
M_t	rotor tilt motion matrix
M_{tip}	tip Mach number
M_{β_p}	flapping motion matrix
M_θ	blade twist and collective pitch matrix
M_ϕ	azimuth motion matrix
N	number of sections on a blade
N_B	number of blades
R	rotor radius, m
R_o	observer-hub distance, m
R_s	observer-blade section distance, m
r	radial position of a blade section midspan, m
S_{pp}	azimuthally averaged acoustic power spectral density (PSD), Pa^2/Hz
$\bar{S}_{\text{pp}}$	instantaneous acoustic PSD, Pa^2/Hz
t	rotor tilt, deg
U_c	convective velocity, m/s
U_e	boundary layer edge velocity, m/s
U_∞	freestream velocity, m/s
u_τ	friction velocity, $(\tau_w/\rho)^{1/2}$, m/s
V_c	ascending speed, m/s
X, Y, Z	source local coordinate system, m
X_1, Y_1, Z_1	observer global coordinate system, m
β_p	blade flap, deg
$\beta_1, \beta_2, \beta_3$	constant scaling parameters
Δr	blade section span, m
δ	boundary layer thickness, m
δ^*	boundary layer displacement thickness, m

*Corresponding author; email: sili@ucdavis.edu.
Presented at the Vertical Flight Society 75th Annual Forum & Technology Display, Philadelphia, PA, May 13–16, 2019. Manuscript received September 2019; accepted February 2020.

DOI: 10.4050/JAHS.65.042006

Θ	momentum thickness, m
θ	blade twist, deg
θ_0	collective pitch, deg
ν	kinematic viscosity, m^2/s
ρ	fluid density, kg/m^3
σ	rotor solidity
τ_w	wall shear stress, Pa
Φ_{pp}	surface pressure spectrum, Pa^2/Hz
ϕ	blade azimuth angle, deg
Ψ	elevation angle, deg
Ω	rotor rotational speed, rad/s
ω	source frequency, rad/s
ω_d	Doppler-shifted frequency, rad/s
OASPL	overall sound pressure level, dB
PWL	sound power level, dB
$\mathrm{SPL}_{i(U/L)}$	blade section (upper or lower surface) sound pressure level, dB
$\mathrm{SPL}_{\mathrm{rotor}}$	rotor sound pressure level, dB

Introduction

Noise from rotorcraft can be categorized into tonal noise and broadband noise by its nature. While rotorcraft tonal noise is typically dominant at low- and midfrequencies, broadband noise covers a wide frequency range, including high frequency to which human ears are sensitive. Historically, less research effort has been devoted to rotorcraft broadband noise compared to its tonal noise. However, rotorcraft broadband noise becomes important when the tonal noise is weak. Recently, interest in broadband noise has been raised with the broader use of rotorcraft and the emergence of urban air mobility vehicle concepts. To demonstrate the importance of rotor broadband noise on traditional helicopters, Snider et al. (Ref. 1) measured helicopter fly-over noise and found that rotor broadband noise is important when it approaches or flies overhead, which significantly contributes to effective perceived noise level. For small-scale rotors, Intaratep et al. (Ref. 2) experimentally showed that broadband noise of a DJI Phantom rotor, especially trailing-edge noise, not only dominates at mid- and high-frequency ranges but also considerably increases from a single rotor to multirotors. In addition, the acoustic measurements by Zawodny et al. (Ref. 3) showed that quadcopter rotors generate significant broadband noise above 1 kHz frequency, and the A-weighted spectrum (Ref. 4) indicated the human ear's high sensitivity at such a frequency range.

Trailing-edge noise is a type of broadband noise that contributes significantly to mid- and high-frequency noise. This noise is generated by the interaction between a turbulent boundary layer flow and a trailing-edge corner on an airfoil section or flat plate. Trailing-edge noise models on an airfoil have been empirically and theoretically developed. A semiempirical Brooks-Pope-Marcolini (BPM) model was developed by Brooks et al. (Ref. 5) and has been widely used to predict airfoil self-noise. Theoretically, Ffowcs Williams and Hall (Ref. 6) provided a trailing-edge noise solution to the Lighthill (Ref. 7) acoustic analogy equation. Likewise, using the theory of Curle (Ref. 8), Amiet (Ref. 9) developed a theoretical model to predict trailing-edge noise on an airfoil.

Schlinker and Amiet (Ref. 10) applied the Amiet airfoil trailing-edge noise model to predict helicopter trailing-edge noise, but their prediction had some critical limitations. First, an airfoil was modeled as a flat plate, which could not well represent actual boundary layer flow properties. Second, the blade section freestream velocity was described as a combination of only rotational and axial freestream velocities, neglecting the induced velocities on the rotor plane. Third, blade noise was assumed to be generated at the rotor hub location, which resulted in errors in the actual source–observer distance. Kim and George (Ref. 11) predicted trailing-edge noise from a hovering rotor from the rotating source formulation of Ffowcs Williams and Hawkings (Ref. 12) with the loading function given in the Amiet model (Ref. 9). In their method, however, each blade was modeled as a point source of a flat plate, and the effect of an angle of attack was neglected. More recently, Blandeau and Joseph (Ref. 13) improved the first limitation of Schlinker and Amiet (Ref. 10) by replacing the flat plate with an airfoil and predicted propeller trailing-edge noise. However, their wall pressure spectrum was obtained from Goody's model (Ref. 14), which was developed for zero pressure gradient flows on a flat plate and is not accurate for airfoil adverse pressure gradient flows. In addition, they assumed that the observer and propeller were in the same vertical plane and neglected the effects of skewed gust. They also considered the noise source as a point source that is located at 75% of the blade radius.

As for the method of accounting for the blade sections as the noise sources, Burley and Brooks (Ref. 15) used coordinate transformations to locate the noise source locations on the blade by including the rotor tilt angle, sectional radius, blade segment pitch angle, and blade azimuthal angle. They applied these coordinate transformations on the BPM airfoil self-noise model (Ref. 5) to predict rotor broadband noise. However, their transformations did not include the blade flapping motion, and the semiempirical BPM model was scaled based on symmetrical NACA0012 airfoils.

In this paper, an improved prediction method named UCD-QuietFly is developed to predict rotor trailing-edge noise. This method utilizes multiple coordinate transformations during the motions of rotor blades to account for each blade section as a noise source and individually compute each blade section's noise contribution to a given observer. The blade twist angle, collective pitch angle, flapping angle, azimuthal angle, sectional radius, and rotor tilt angle are included in the coordinate transformation. This method relates the flow physics at the trailing-edge noise to sound propagation. The new model combines blade element momentum theory (BEMT), XFOIL boundary-layer panel code, and a recently developed empirical wall pressure spectrum model (Ref. 16) to accurately obtain the source of trailing-edge noise at given flight conditions of rotorcraft. Following its development, UCD-QuietFly is validated against airfoil trailing-edge noise and rotor noise measurements in hover.

For the airfoil section, the effects of flow Mach number, angle of attack, and chord length on the trailing-edge noise come from studies by other researchers. Hutcheson and Brooks (Ref. 17) computationally and experimentally showed that airfoil trailing-edge noise is well scaled with the fifth power of the flow Mach number and that the angle of attack only affects low-frequency noise. For the same effective angle of attack, Brooks et al. (Ref. 5) experimentally showed, with a boundary-layer tripped airfoil, that a larger chord length increased the noise level and shifted the level peak to a lower frequency. Lee (Ref. 18) also studied the effect of the airfoil shape on trailing-edge noise using a TNO-Blake model. He identified the noise source region for different airfoils at different conditions and showed that the suction side contributes to the low-frequency noise and the pressure side contributes to the high-frequency noise. On rotorcraft, Chou and George (Ref. 19) found that collective pitch angle has a large effect on low-frequency and midfrequency noise while it has a negligible effect on high-frequency noise.

In the second part of this paper, UCD-QuietFly is used to study the effects of rotor tip Mach number, collective pitch, blade twist, rotor solidity, rotor radius, ascending speed, disk loading, and number of blades on rotor trailing-edge noise. Finally, the rotor noise directivity is analyzed, and a semianalytic equation is proposed to represent the geometric attenuation and the directivity of rotorcraft trailing-edge noise.

Method

In this section, the formulations of UCD-QuietFly are presented. We use Amiet's power spectral density (PSD) $\overline{S}_{\rm pp}$ (Ref. 9) at an observer location (X, Y, Z) of each surface of an airfoil as

$$\overline{S}_{\rm pp} = \frac{1}{32\pi^2}\left(\frac{\omega_d c Z}{c_o \epsilon^2}\right)^2 \Delta r |L|^2 l_r \Phi_{\rm pp}, \tag{1}$$

where $\epsilon^2 = X^2 + \beta^2(Y^2 + Z^2)$, $\beta^2 = 1 - M^2$, ω_d is the Doppler-shifted frequency, c is the chord length, c_o is the speed of sound, Δr is the blade sectional span, L is the loading term, l_r is the spanwise turbulence correction length, and $\Phi_{\rm pp}$ is the wall pressure spectrum. The blade sectional local coordinate is shown in Fig. 1. For each section on a blade, the origin of the local coordinate is located at the midspan of the section.

The motion of rotor blades is included in the coordinate transformation. The twist angle matrix M_θ, azimuth motion matrix M_ϕ, tilt motion matrix M_t, and flapping motion matrix M_{β_p} transform the geographical global coordinate (X_1, Y_1, Y_1) shown in Fig. 2 to the sectional local coordinate (X, Y, Z) shown in Fig. 1.

$$\begin{bmatrix} X \\ Y \\ Z \end{bmatrix} = M_\theta M_\phi \left[M_t \begin{bmatrix} X_1 \\ Y_1 \\ Z_1 \end{bmatrix} + M_{\beta_p} \right] \tag{2}$$

where M_θ, M_ϕ, M_t, and M_{β_p} are defined as

$$M_\theta = \begin{bmatrix} \cos(\theta_0+\theta) & 0 & \sin(\theta_0+\theta) \\ 0 & 1 & 0 \\ -\sin(\theta_0+\theta) & 0 & \cos(\theta_0+\theta) \end{bmatrix},$$

$$M_\phi = \begin{bmatrix} \sin\phi & -\cos\phi & 0 \\ \cos\phi & \sin\phi & 0 \\ 0 & 0 & 1 \end{bmatrix},$$

$$M_t = \begin{bmatrix} \cos t & 0 & \sin t \\ 0 & 1 & 0 \\ -\sin t & 0 & \cos t \end{bmatrix},$$

$$M_{\beta_p} = \begin{bmatrix} -r\sin\beta_p\cos\phi \\ -r\sin\beta_p\sin\phi \\ r\cos\beta_p \end{bmatrix}. \tag{3}$$

where θ_0 describes the collective pitch angle that varies with the rotor thrust, θ describes the twist angle, ϕ describes the azimuth angle, t describes the tilt angle with positive angle tilting up, r describes the blade sectional distance from the hub, and β_p describes the flapping angle. To the authors' best knowledge, none of the earlier research included the entire blade motions, with the flapping, collective pitch, cyclic pitch, and twist angles, in the prediction of rotor trailing-edge noise. Even though cyclic flapping and pitch angles are not present in hover, they should be included in forward flight to accurately prescribe blade motion and trailing-edge location. Cyclic flapping and cyclic pitch angles are combined into β_p and θ_0 as the time-dependent quantities. The angles are described in Figs. 2 and 3. With the directions of positive angles defined the counterclockwise direction, the collective pitch angle is between the rotor hub plane and the blade root chord plane, and the twist angle is between the root chord plane and the section chord plane. In other words, the collective pitch angle is a pilot's control input that adjusts the blade's feathering motion, while the twist angle varies for different blade sections.

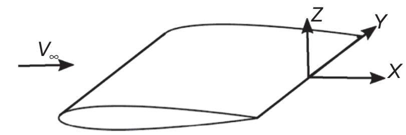

Fig. 1. Blade section local coordinate.

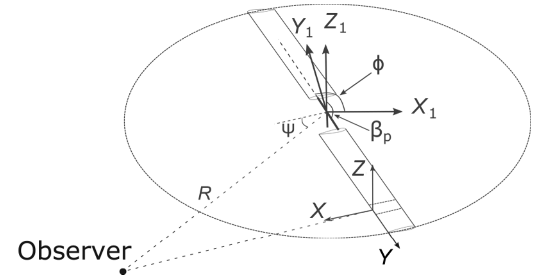

Fig. 2. Rotor local and global coordinates for an observer.

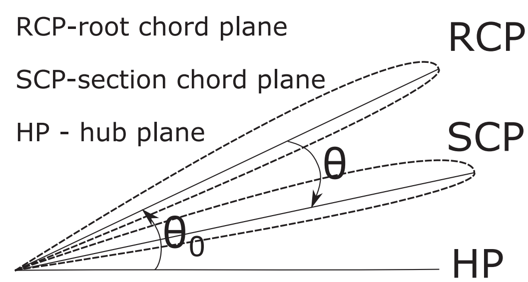

Fig. 3. Blade collective pitch and twist. Collective pitch angle (θ_0) measures from the rotor hub plane to the root chord plane, and twist angle (θ) measures from the root chord plane to the section chord plane, with positive angles in the counterclockwise direction.

The PSD of each section changes with the azimuth angle; hence, it is azimuthally averaged by

$$S_{\rm pp} = \frac{N_B}{2\pi}\int_0^{2\pi}\left(\frac{\omega}{\omega_d}\right)^2 \overline{S}_{\rm pp} d\phi, \tag{4}$$

in which the Doppler-shifted frequency ω_d at the observer is related to the source frequency ω using

$$\frac{\omega_d}{\omega} = \frac{1}{1 + M_r\left(\dfrac{X}{R_s}\right)}. \tag{5}$$

Note that $M_r = \Omega r / c_o$ is the rotational Mach number of the blade section. R_s is the distance between the blade section and an observer, and X has the direction pointing from leading edge to trailing edge, which is parallel to the chord of an airfoil shown in Figs. 1 and 2. Substituting Eq. (1) and Eq. (5) into Eq. (4) and expanding the terms gives the acoustic PSD generated from each blade section as

$$S_{\rm pp} = \left(\frac{\omega}{c_o}\right)^2 c^2 \triangle r \left(\frac{1}{32\pi^2}\right)\frac{B}{2\pi}\int_0^{2\pi} D_\phi |L|^2 l_r \Phi_{\rm pp} d\phi. \tag{6}$$

The directivity term is given as $D_\phi = (Z/\epsilon^2)^2$, where ϵ is defined in Eq. (1). The local coordinate of Z and ϵ must be found by taking the coordinate transformations in Eqs. (2) and (3) from the global coordinate.

A detailed equation of the directivity term D_ϕ in terms of the global coordinate system (X_1, Y_1, Z_1) is provided in the Appendix.

The loading term L is given by Schlinker and Amiet (Ref. 10) as

$$|L| = \frac{1}{\Lambda}\left|e^{i2\Lambda}\left[1-(1+i)\,E^*(2(\overline{K}+\overline{\mu}M+\overline{\gamma}))\right.\right.$$
$$\left.\left.+\,e^{-i2\Lambda}\sqrt{\frac{K+\mu M+\gamma}{\mu x/\epsilon+\gamma}}\,(1+i)\,E^*\left(2\left(\overline{\mu}x/\epsilon+\overline{\gamma}\right)\right)\right]\right| \quad (7)$$

where $\Lambda = \overline{k}_x - \overline{\mu}x/\epsilon + \overline{\mu}M$, $K = \omega_d/U_c$, $\mu = \omega_d M/U\beta^2$, $\gamma^2 = (\mu/\epsilon)^2(x^2+\beta^2 z^2)$, and E^* represent the complex conjugate of a Fresnel integral. The turbulence convective velocity and spanwise turbulence length scale are defined as $U_c = 0.8U_\infty$ and $l_r = 1.6U_c/\omega$, respectively.

The remaining wall pressure spectrum Φ_{pp} is obtained by a recently developed empirical wall pressure spectrum model for nonzero gradient flows, Lee's model (Ref. 16), as

$$\frac{\Phi_{\mathrm{pp}}(\omega)U_e}{\tau_w^2\delta^*} = \frac{\max(a,(0.25\beta_c-0.52)a)\left(\frac{\omega\delta^*}{U_e}\right)^2}{\left[4.76\left(\frac{\omega\delta^*}{U_e}\right)^{0.75}+d^*\right]^e+\left[8.8R_T^{-0.57}\left(\frac{\omega\delta^*}{U_e}\right)\right]^{h^*}} \quad (8)$$

where $\beta_c = (\Theta/\tau_w)\,|dp/dx|$, $a = 2.28\Delta^2(6.13\Delta^{-0.75}+d)^e[4.2(\Pi/\Delta)+1]$, $\Delta = \delta/\delta^*$, $\Pi = 0.8(\beta_c+0.5)^{3/4}$, $e = 3.7+1.5\beta_c$, $d = 4.76(1.4/\Delta)^{0.75}[0.375e-1]$, $R_T = (\delta/U_e)(\nu/u_\tau^2)$, $h^* = \min(3,(0.139+3.1043\beta_c))+7$, and if $(\beta_c < 0.5)$, $d^* = \max(1.0, 1.5d)$, otherwise $d^* = d$.

Finally, the far-field narrow-band sound pressure level (SPL) for one side of the ith section is calculated from the power spectral density S_{pp} as

$$\mathrm{SPL}_{i(U/L)} = 10\log_{10}\left(\frac{2\pi S_{\mathrm{pp}}}{(2\times10^{-5})^2}\right) \quad (9)$$

where U and L represent the upper and lower surfaces of an airfoil, respectively. The rotor's total SPL is logarithmically summed to be

$$\mathrm{SPL}_{\mathrm{rotor}} = 10\log_{10}\sum_{i=1}^{N}\left(10^{0.1\mathrm{SPL}_{iU}}+10^{0.1\mathrm{SPL}_{iL}}\right) \quad (10)$$

where N is the total number of sections. Since some prediction and measurement results presented in this paper are expressed in one-third octave band sound pressure levels ($\mathrm{SPL}_{1/3}$) and overall sound pressure levels (OASPL), the conversions from the narrow-band sound pressure level ($\mathrm{SPL}_{\mathrm{rotor}}$) in Eq. (10) to the other two noise metrics are presented in the Appendix. OASPL is integrated in the frequency range of 0.1−10 kHz.

During the prediction process, the blade sectional freestream velocity and angle of attack are obtained from the BEMT in hover, and the boundary-layer flow parameters, which are inputs to Eq. (8), are obtained from XFOIL (Ref. 20).

Results

The predictions of trailing-edge noise from UCD-QuietFly are first validated against measurement data for airfoil and helicopter noise. After the validation, this prediction tool is used to perform trend analyses of trailing-edge noise associated with rotor design and operating parameters, such as the rotor tip Mach number, ascending speed, radius, blade collective pitch angle, twist angle, rotor solidity, disk loading, and number of blades. The detailed flow physics behind this noise trend is also discussed. A semianalytic equation is obtained from a noise map on the plane observers.

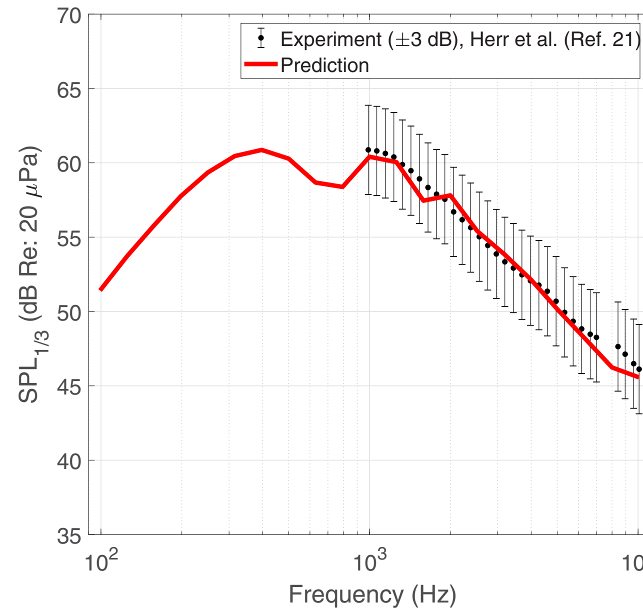

Fig. 4. Validation of airfoil trailing-edge noise prediction against measurement (Ref. 21).

Validation

This section first shows the validation of airfoil trailing-edge noise predictions to demonstrate the accuracy of the numerical method on one blade section. Next, two experimental cases of hovering helicopters are used to demonstrate the validity of UCD-QuietFly. In addition, the UCD-QuietFly predictions are compared with the predictions by Kim and George (Ref. 11). For the validations against the two rotorcraft cases, 40 sections are used on each blade and 240 airfoil panels are used in the XFOIL. The computational time to obtain the noise level for one observer is 65 s on a personal desktop computer with an Intel i7-9700 Processor, 8 cores, and 16 GB RAM.

Airfoil trailing-edge noise validation. Airfoil trailing-edge noise is predicted and compared with the measurement, which was reported in Benchmark Problems for Airframe Noise Computations (BANC) (Ref. 21). Table 1 describes the airfoil test conditions. For this airfoil validation case, the turbulence convective velocity $U_c = 0.7U_\infty$ and spanwise turbulence lengthscale $l_r = 1.0U_c/\omega$ are used (Ref. 22).

One-third octave band sound pressure levels (SPLs) of airfoil trailing-edge noise prediction and the measurement are presented in Fig. 4 in which error bars of ±3 dB are included. The prediction has a good match with the measurement at an entire frequency range, which demonstrates the validity of the numerical approach involving the boundary-layer flow parameters from XFOIL, Lee's wall pressure spectrum model in Eq. (8), and the Amiet model in Eq. (1).

Rotor tailing-edge noise validation case 1. In Table 1, the helicopter configuration in the experiment conducted by Johnson and Katz (Ref. 23) is shown, where the observer is 5 rotor diameters from the hub with an elevation angle of $\Psi = 26.7°$. In the experiment, a UH-1B helicopter was used.

The UCD-QuietFly prediction of the Johnson case is presented in Fig. 5 along with the measurement and the prediction by Kim and George (Ref. 11). The results show that UCD-QuietFly has a good match with the measurement in the mid- and high-frequency range in which

Table 1. Test conditions for validation cases

Item	Case 1: Airfoil BANC (Ref. 21)	Item	Case 2: Model rotor Johnson (Ref. 23)	Case 3: Helicopter Leverton (Ref. 24)
Airfoil	NACA0012	Radius (m)	6.7056	8.5
Chord length (m)	0.4	Airfoil	NACA0012	NACA0012
Span (m)	1.0	Number of blade	2	2
(X, Y, Z) (m)	(0.0, 0.0, 1.0)	Linear twist (deg)	−10	−8
Transition[a]	S[b]: 0.06, P[b]: 0.07	Solidity	0.0506	0.0312
U_∞ (m/s)	53.0	(X_1, Y_1, Z_1) (m)	(60.69, 0, −30.48)	(19.7, 0, −73.6)
Angle of attack (deg)	6	(R_o, Ψ) (m, deg)	(67.91, −26.7)	(76.19, 75)
		C_T	0.0036	0.002
		M_{tip}	0.67	0.47

[a]Fixed transition position (x/c).

[b]S: suction side, P: pressure side.

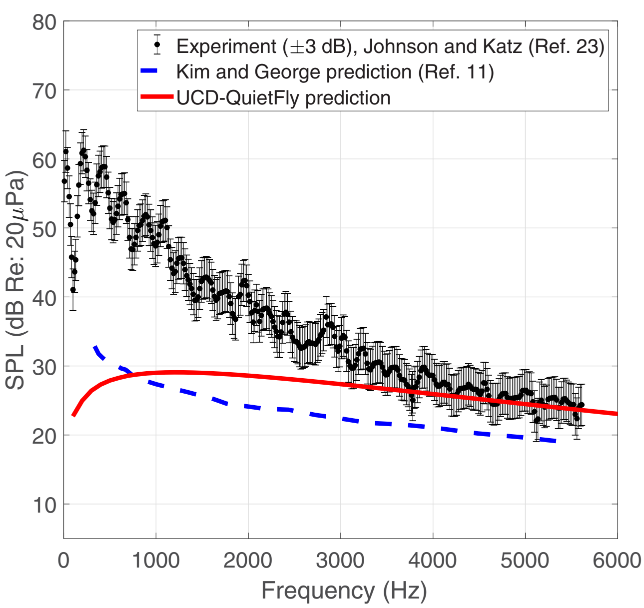

Fig. 5. Comparison of UCD-QuietFly prediction with measurement by Johnson and Katz (Ref. 23) and prediction by Kim and George (Ref. 11).

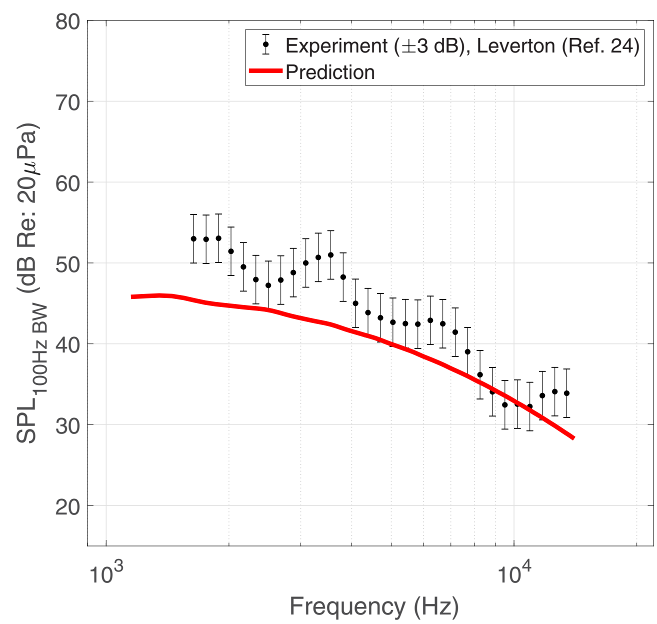

Fig. 6. Comparison of UCD-QuietFly prediction with measurement by Leverton (Ref. 24).

trailing-edge noise is expected to be the dominant noise source. In addition, Fig. 5 shows that UCD-QuietFly is more accurate than Kim and George's prediction for the entire frequency range.

Rotor tailing-edge noise validation case 2. Table 1 includes Leverton's (Ref. 24) measured noise from a model rotor at an observer located at 4.5 rotor diameters from the hub with an elevation angle of $\Psi = 75°$.

The prediction of the Leverton case is presented in Fig. 6. Note that the SPL in Fig. 6 has a constant frequency bandwidth of 100 Hz and sums the 1-Hz energy in each band. It is also shown that the prediction exhibits similar trends with the data. It is shown that the prediction is in good agreement with the data at high frequencies. The prediction does not capture the local noise maximum at 2.5–4 kHz. It is thought that this local noise maximum is generated from different noise sources such as trailing-edge bluntness noise, which can be predicted by the semiempirical trailing-edge bluntness noise term in the BPM model developed by Brooks et al. (Ref. 5).

Table 2. Range of parameters

Parameter	Start	End	Base
M_{tip}	0.45	0.8	0.67
θ_0(deg)	11	18	13.52
θ(deg)	−13	−4	−10
σ	0.0507	0.1200	0.0507
R (m)	2.3	8.0	6.7056
V_c (m/s)	0	9	0

Rotor parameters trend analysis

In this subsection, UCD-QuietFly is used to investigate the trend of rotor trailing-edge noise with different parameters. The six parameters studied are listed in Table 2, and other constant conditions are shown in Table 3. Each parameter is analyzed from the start to the end values, whereas other parameters are kept at the base values. For each parameter, 20 values were selected. An observer is located at one base rotor diameter from the hub with −90° elevation angles.

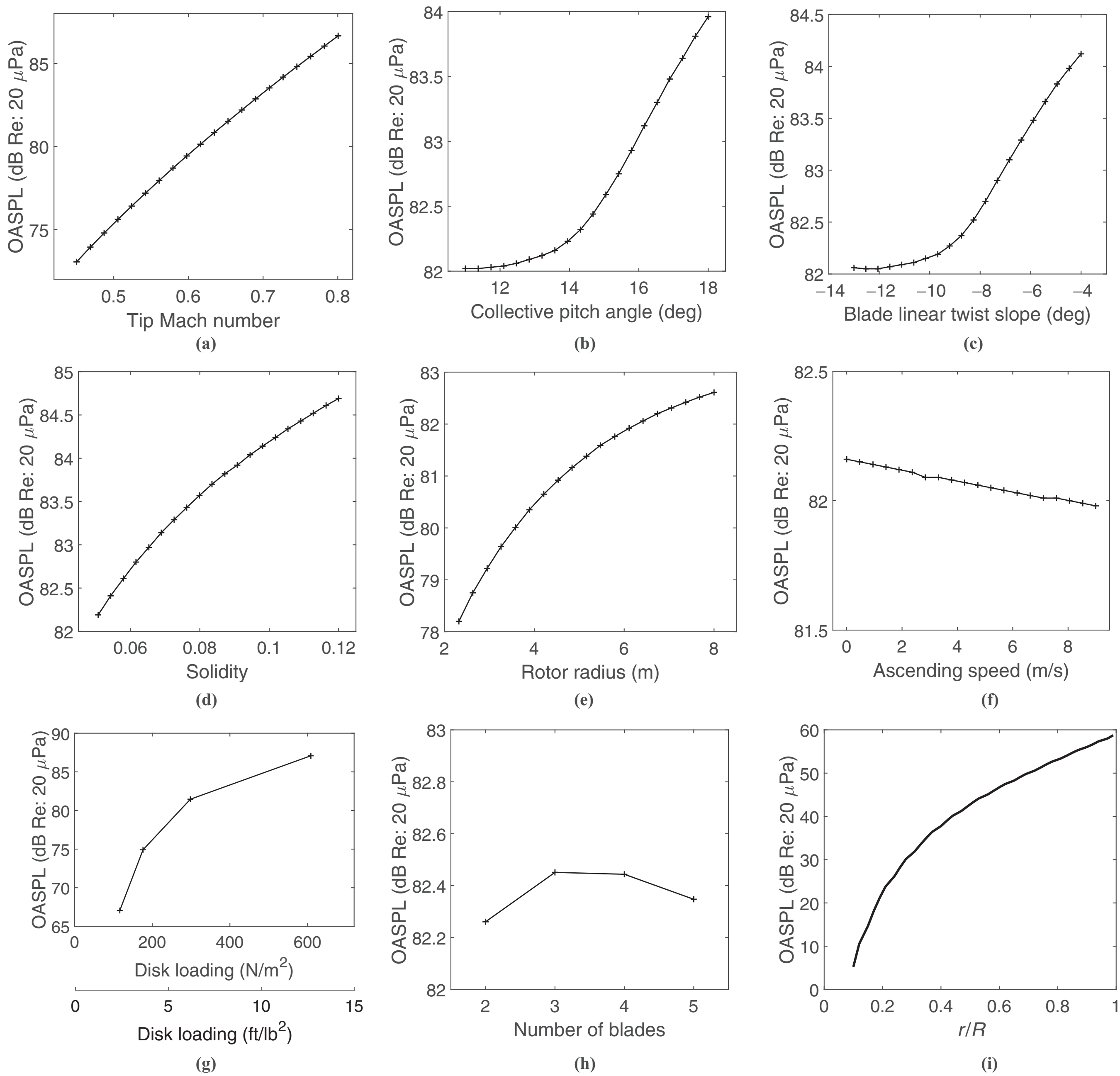

Fig. 7. OASPL trend with parameters: (a) tip Mach number, (b) collective pitch angle, (c) blade linear twist slope, (d) rotor solidity, (e) rotor radius, (f) rotor ascending speed, (g) disk loading, (h) number of blades, and (i) sectional noise contribution from one blade.

Table 3. Constant conditions

Item	Value
Airfoil	NACA0012
(R_o, Ψ)(m, deg)	(13.4112, −90)
N_B	2

First, the trends of the OASPL associated with the rotorcraft design and operating parameters are presented in Fig. 7. It is seen that the OASPL increases with increasing tip Mach number, collective pitch angle, blade twist angle, rotor solidity, rotor radius, and disk loading, but the ascending speed and the number of blades with the constant solidity have negligible effects on rotor trailing-edge noise. The blade pitch angle, twist angle, and rotor solidity change OASPL only by about 2 dB within the specified ranges. The rotor radius changes OASPL by about 5 dB. Among the studied parameters, the tip Mach number is found to be the dominant factor in rotorcraft trailing-edge noise. Detailed studies of the parameters are provided in the following sections to show the narrowband sound pressure levels and the flow physics in terms of the boundary layer parameters.

With a constant rotor radius, the OASPL contribution from each blade section is plotted in Fig. 7(i). Since the tip sections have a higher velocity than the root sections, the trailing-edge noise level from the tip sections is higher.

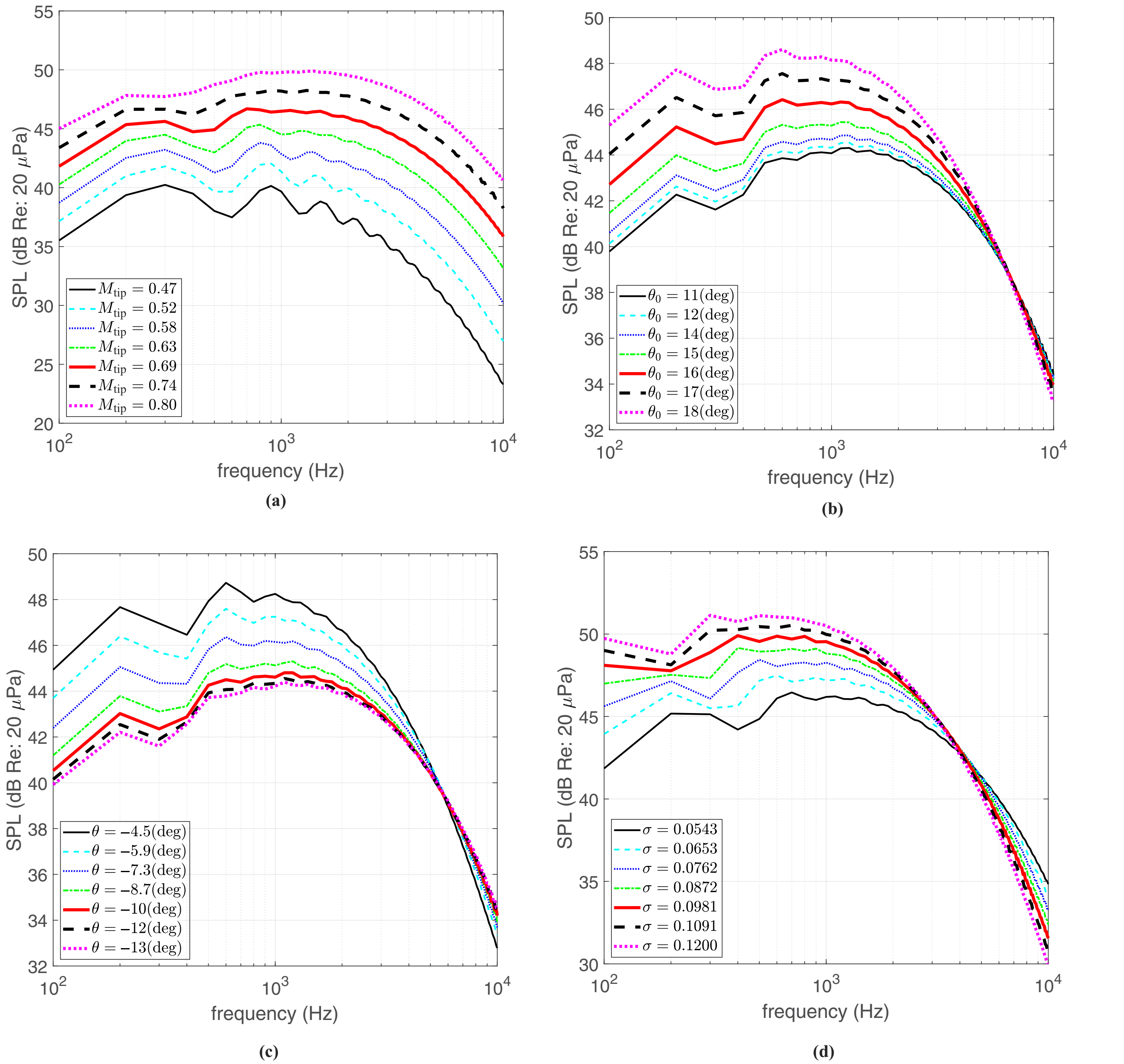

Fig. 8. Narrow-band SPL trends with design parameters: (a) tip Mach number, (b) collective pitch angle, (c) twist slope, and (d) chord length.

Effect of rotor tip Mach number. The trend of narrow-band sound pressure level associated with the rotor tip Mach number is shown in Fig. 8(a). It is shown that the narrow-band SPL increases with increases to the tip Mach number for the entire frequency range. This trend is explained by the boundary layer parameters measured near the trailing edge ($x/c = 0.99$) at 90% rotor radius position as shown in Fig. 9. The noise increase is mainly accounted for by the increase in the boundary layer edge velocity U_e and the pressure gradient dp/dx near the trailing edge. The higher tip Mach number gives a higher boundary layer edge velocity and higher convection velocity. According to Eq. (8), the strength of the wall pressure spectrum is proportional to the boundary layer edge velocity; hence, the higher wall pressure spectrum results in a higher noise level. In addition to the increase in the magnitude of SPL, the increased tip Mach number shifts the spectral peak to a higher frequency.

In Fig. 10(a), the SPL is scaled with the tip Mach number, and the frequency is normalized with the tip Mach number to collapse the maximum peak frequency. It is found that SPLs collapse very well into a single line, especially for high Mach number cases with the 4.7th power of the tip Mach number and the frequency scaling of $f * 0.8/M_{\rm tip}$. This frequency scaling has the same physical meaning as the Strouhal number (fL/U_∞); however, on a rotor blade, the characteristic length (L) and freestream velocity (U_∞) are not constant values for different sections. Therefore, a frequency scaling of $f * 0.8/M_{\rm tip}$ is chosen over the Strouhal number, where $0.8/M_{\rm tip} = 0.8c_0/U_{\rm tip}$ is a consistent reference value for the blade sections, which also serves the same purpose as L/U_∞ in the Strouhal number. The rotor tip Mach number scaling between two rotors is provided in Eq. (11), which is close to the flow Mach number's fifth power scaling for airfoil trailing-edge noise as suggested by Hutcheson

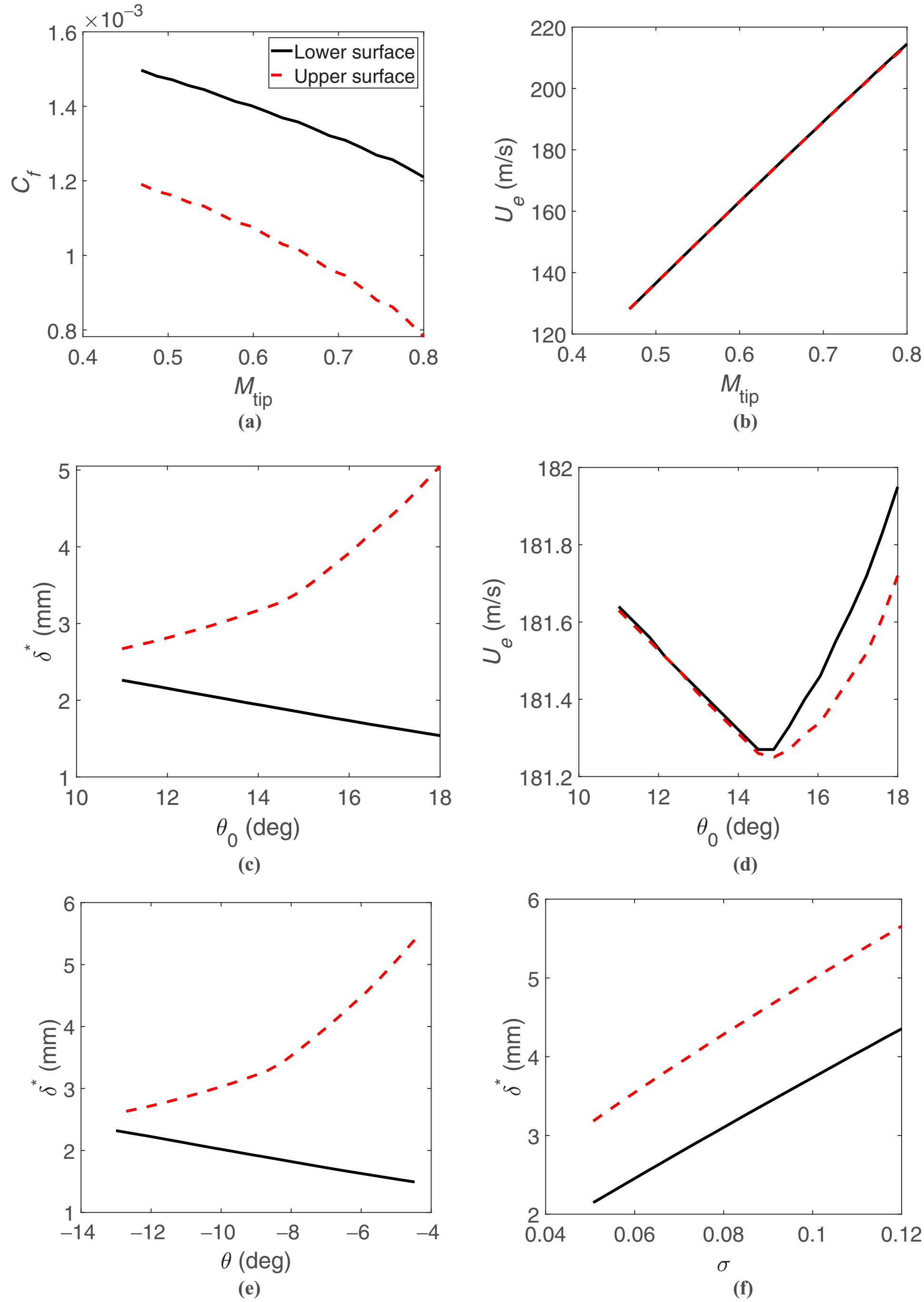

Fig. 9. Boundary layer parameters measured near the trailing edge ($x/c = 0.99$) at 90% rotor radius: (a) M_{tip} versus C_f, (b) M_{tip} versus U_e, (c) θ_0 versus δ^*, (d) θ_0 versus U_e, (e) θ versus δ^*, and (f) σ versus δ^*.

and Brooks (Ref. 17).

$$\mathrm{SPL}_{\mathrm{rotor}} = \mathrm{SPL}_{\mathrm{rotor,\,ref}} + 10\log_{10}\left[\left(\frac{M_{\mathrm{tip}}}{M_{\mathrm{tip,ref}}}\right)^{4.7}\right] \tag{11}$$

It is also found that the scaling factor varies in the approximate range of 4.5–5.0 as a function of the collective pitch angle as shown in Fig 10(c), and it has the local maximum of 5.0 at $\theta_0 = 10^\circ$ as presented in 10(b) where the rotor tip has the angle of attack close to 0° since $\theta = -10^\circ$. Therefore, regarding the typical collective pitch and blade twist for the operation and design of helicopters, the tip Mach number scaling ranges from 4.5 to 5.0 with an average of 4.7.

Effect of blade collective pitch. Collective pitch angle changes the angle of attack on the entire blade. Figure 8(b) shows that increasing collective pitch angle gives higher low-frequency noise while high-frequency (larger than 5 kHz) noise remains unchanged. In Fig. 9(c), as the angle of attack increases, the boundary-layer displacement thickness increases on the upper surface and decreases on the lower surface. It is also found that the change in the edge velocity U_e is small. Although Hutcheson and

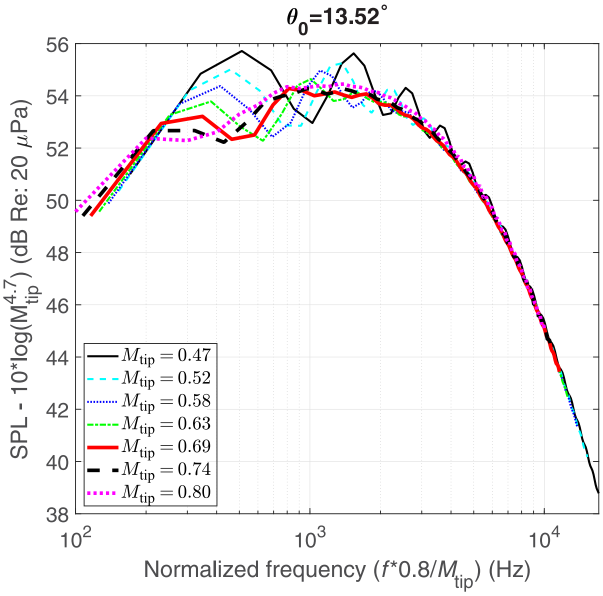

(a)

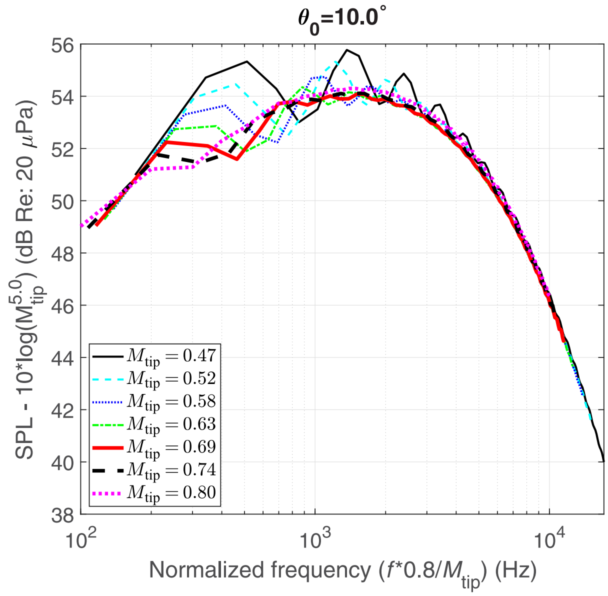

(b)

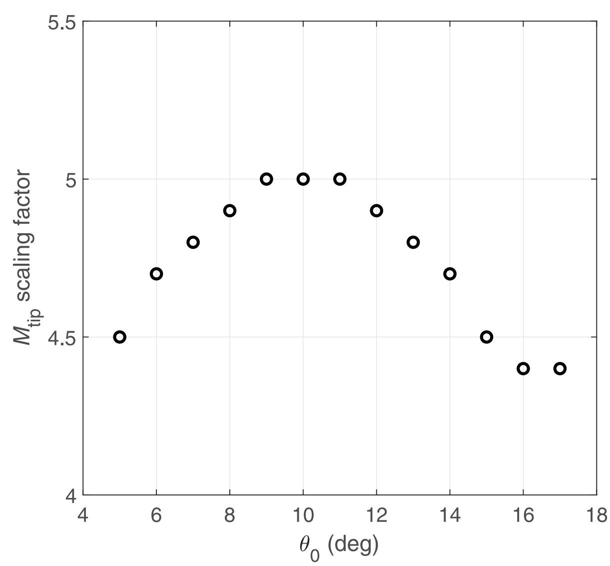

(c)

Fig. 10. Scaled SPL with tip Mach number: (a) $\theta_0 = 13.52°$, (b) $\theta_0 = 10.0°$, and (c) scaling factor for various collective pitch angles with blade twist fixed at $-10°$.

Brooks (Ref. 17) showed that the angle of attack only affects noise with frequencies lower than 1 kHz, Fig. 8(b) demonstrates the collective pitch angle's influence on frequency lower than 5 kHz for rotorcraft noise.

Chou and George's results (Ref. 19), based on the Kim and George method (Ref. 11), showed that the effect of the collective pitch on the low-frequency (100 Hz) and the midfrequency (1000 Hz) noise were the same. However, it is shown that the effect on low-frequency noise is larger than that on midfrequency noise.

Effect of blade twist. Unlike the collective pitch angle, blade linear twist angle varies with the blade radial position. Figure 8(c) shows the SPL as a function of the linear twist slope from the root to the tip. The noise trend with the twist angle is similar to the trend for the collective pitch angle. In fact, the behaviors of the boundary-layer parameters, shown in Fig. 9(e), are similar to those for the collective pitch angle.

Effect of rotor solidity. Figure 8(d) shows the SPLs for the various rotor solidity, which is varied by the chord length as the rotor radius and number of blades are fixed. The increase in chord length results in higher low-frequency noise, while the high-frequency noise remains unchanged. Since the boundary layer develops further with a longer chord length, the boundary layer becomes thicker, especially on the upper surface, as shown in Fig. 9(e), which accounts for the increase in low-frequency noise. In addition, the peak level shifts to lower frequencies as the rotor solidity is increased, which agrees with the effect of a chord length on airfoil noise (Ref. 5).

Effect of rotor radius. Figure 11(a) shows the SPLs as a function of the blade radius with the same tip Mach number. It is shown that the increased rotor radius gives higher sound pressure levels in the entire frequency range. The boundary-layer parameter changes measured near

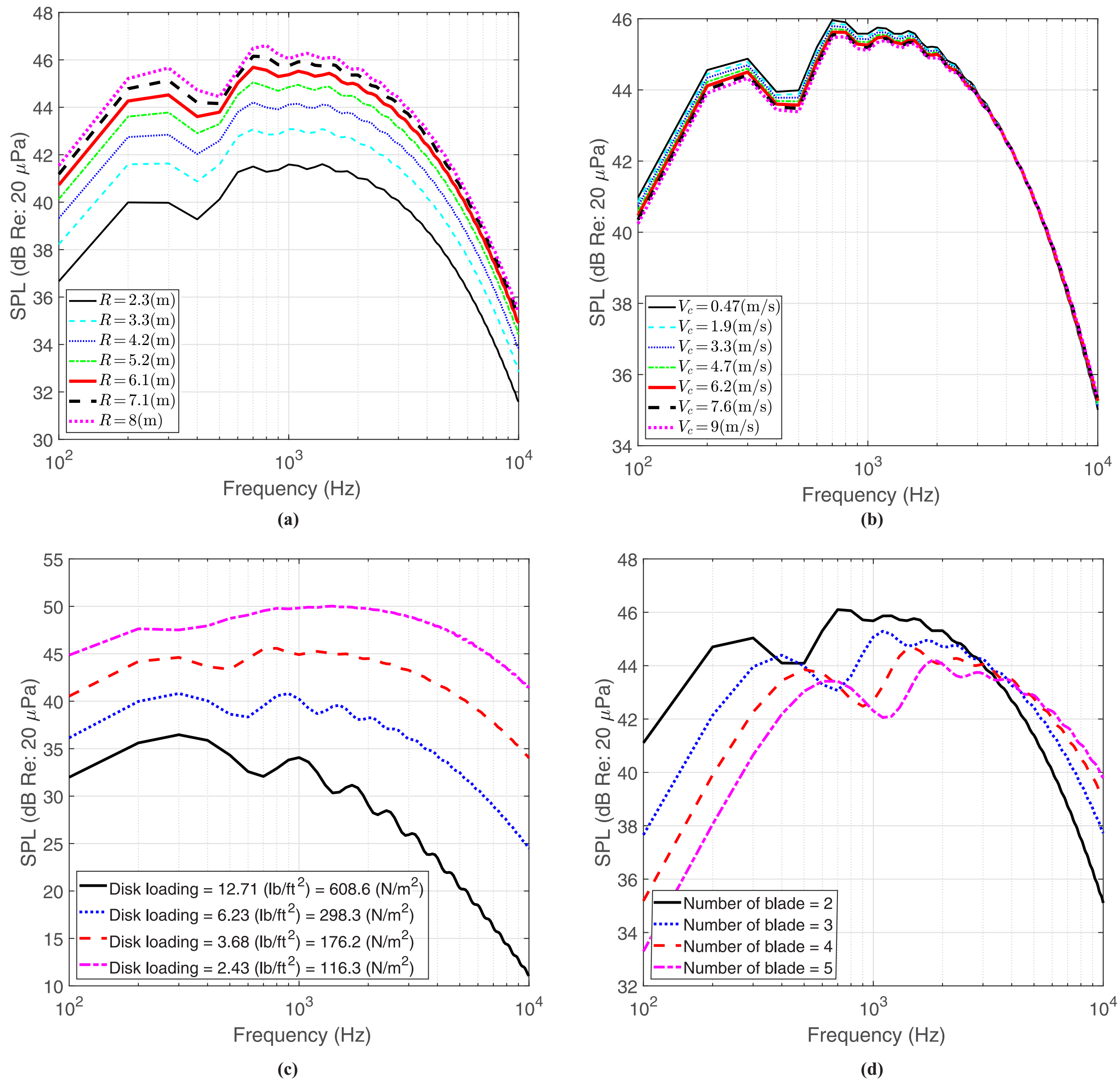

Fig. 11. Narrow-band SPL trends with design parameters: (a) rotor radius, (b) rotor ascending speed, (c) disk loading, and (d) number of blades.

the trailing edge ($x/c = 0.99$) at 90% rotor radius are small, as shown in Fig. 12, since the tip Mach number is kept constant. The main factor accounting for the noise increase is the span increase with increasing the rotor radius. In other words, the source region is increased by increasing the blade radius.

Effect of rotor ascending speed. Figure 11(b) shows the SPLs as a function of the rotor climb or ascending speed. An increased ascending speed slightly increases the noise level. The effect is small compared to the other rotor parameters since the variation of the local angle of attack is small within the limited realistic ascending speed range, which is 9 m/s for this rotor. Figure 12 confirms that the changes in the boundary-layer parameters are small with the ascending speed.

Effect of disk loading. As for the investigation of the effect of rotor disk loading, the rotor thrust is fixed at 23,000 N, whereas the rotor radius and the collective pitch are varied to match the four selected disk loading values, which is essentially the effect of a combination of rotor radius and collective pitch. The effect of disk loading on the rotor trailing-edge noise is presented in Fig. 11(c), where the noise level increases with the decreasing disk loading since the lower disk loading results in the larger rotor radius and, therefore, the larger airfoil span. It is worthwhile noting that tonal noise is increased with the increasing disk loading (Ref. 25) due to the increased loading on the blades, which is opposite to the observation of rotor trailing-edge noise.

Effect of number of blades. In the study of the effect of the number of blades on rotor trailing-edge noise, all the parameters in Table 2 are fixed at the base values while the chord length is varied for the different number of blades to ensure the solidity to be the same. Figure 11(d) shows that when the number of blades is increased, or the chord length decreased, the low- to midfrequency trailing-edge noise is decreased while the high-frequency noise is increased. OASPL does not change noticeably with the number of blades, as shown in Fig. 7(h), since the decrease of the

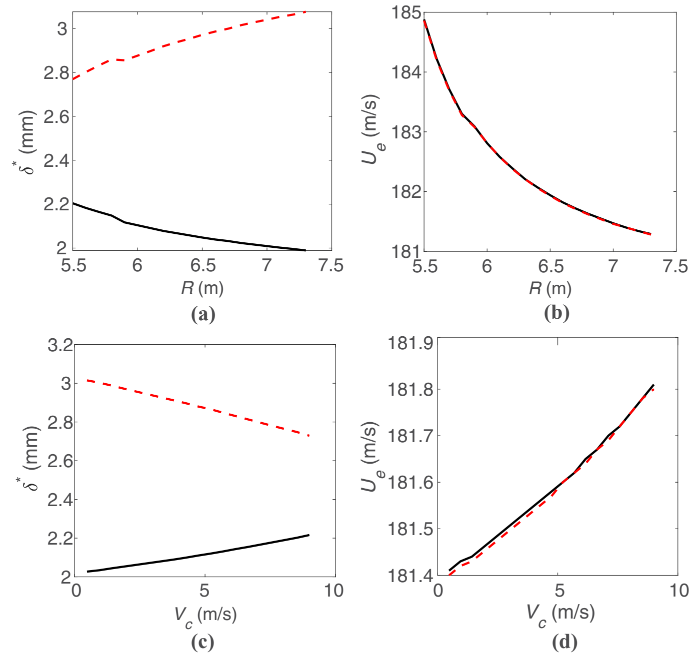

Fig. 12. Boundary layer parameters measured near the trailing edge ($x/c = 0.99$) at 90% rotor radius: (a) R versus δ^*, (b) R versus U_e, (c) V_c versus δ^*, and (d) V_c versus U_e.

low-frequency noise level is offset by the increase of the high-frequency, but the narrow-band SPL change is large, and human perception of noise could be different depending on the number of blades. It is interesting to note that rotor tonal noise is decreased by increasing the number of blades since the loading noise is decreased as the lifting force is distributed on more blades (Ref. 26).

Rotor geometric attenuation and directivity

The geometric attenuation and directivity pattern of rotor trailing-edge noise are studied, and a semianalytic equation is obtained to relate the OASPL at any observer location to a reference location of one rotor diameter with a -90° elevation angle. Using the base values in Table 2, the OASPL is predicted by UCD-QuietFly on the X_1Y_1 and X_1Z_1 planes shown in Figs. 13(a) and 13(b). Table 4 provides the detailed coordinate ranges about these two planes. The dipole directivity is shown in Fig. 13(a) when the noise levels are viewed from the side of rotorcraft. When the noise levels are viewed from the top in Fig. 13(b), the noise contours have a monopole directivity.

Table 4. Geometric attenuation and directivity

	X_1Y_1	X_1Z_1
X_1 range (m)	[−70,70]	[−30,30]
Y_1 range (m)	[−70,70]	NA
Z_1 range (m)	NA	[−100,−10]
Grid size (m)	10	5
Distance to hub (m)	−26.8	0

The ISO standard (Ref. 27) gives the geometric attenuation of a point source as shown in Eq. (12), where $\mathrm{PWL_{ref}}$ is the sound power level at a point source.

$$\mathrm{SPL} = \mathrm{PWL_{ref}} - [20\log(R) + 11] \tag{12}$$

However, Eq. (12) cannot be directly applied to predict rotorcraft noise in the far field since the noise source is not a point source. In addition, rotor trailing-edge noise has a dipole directivity, which should be included in far-field noise predictions. The rotor geometric attenuation equation is proposed to be a form of Eq. (13) in which the first term accounts for the directivity at one rotor diameter distance whereas the second term couples the effect of the attenuation and directivity.

$$\mathrm{OASPL} = (\sin^{\beta_1}|\phi|)\mathrm{OASPL_{ref}} - [\beta_2 + \beta_3(1 - \sin|\phi|)]\log\left(\frac{R_0}{d}\right) \tag{13}$$

The constants β_1, β_2, and β_3 are determined by minimizing the difference between this equation and the noise predicted on the X_1Y_1 and X_1Z_1 planes. $\mathrm{OASPL_{ref}}$ is the OASPL at one rotor diameter with a -90° elevation angle. Based on the prediction results shown in Figs. 13(a) and 13(b), the quasi-Newton minimization method is used to find the three

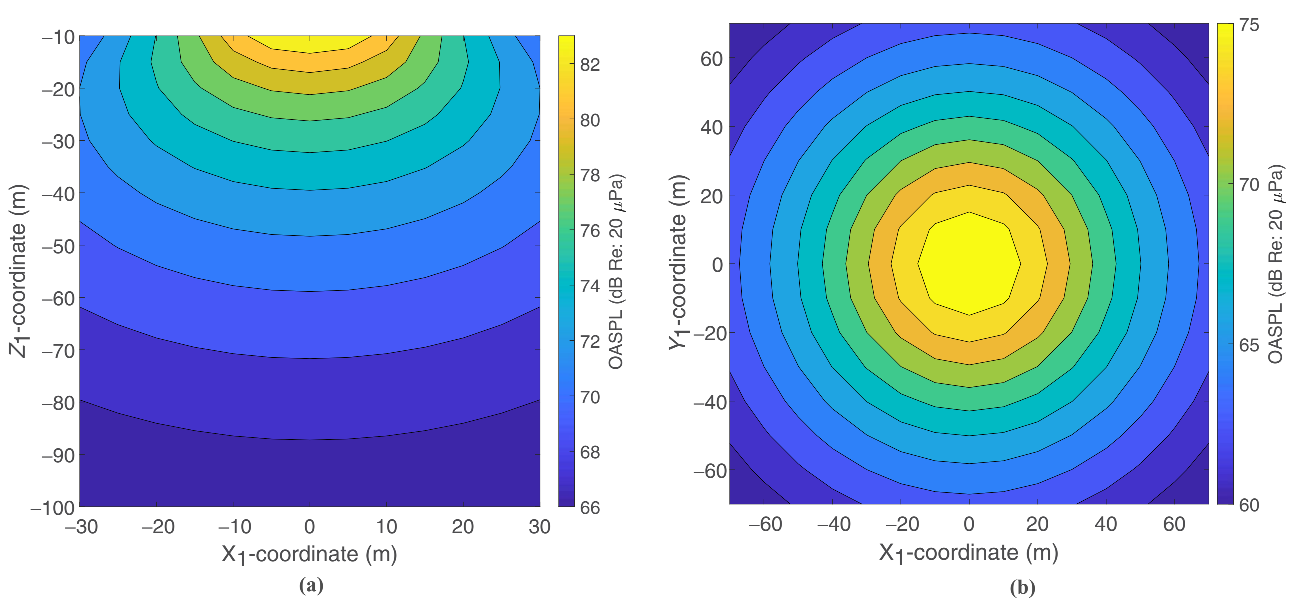

Fig. 13. OASPL obtained from UCD-QuietFly on (a) X_1Z_1 plane and (b) X_1Y_1 plane.

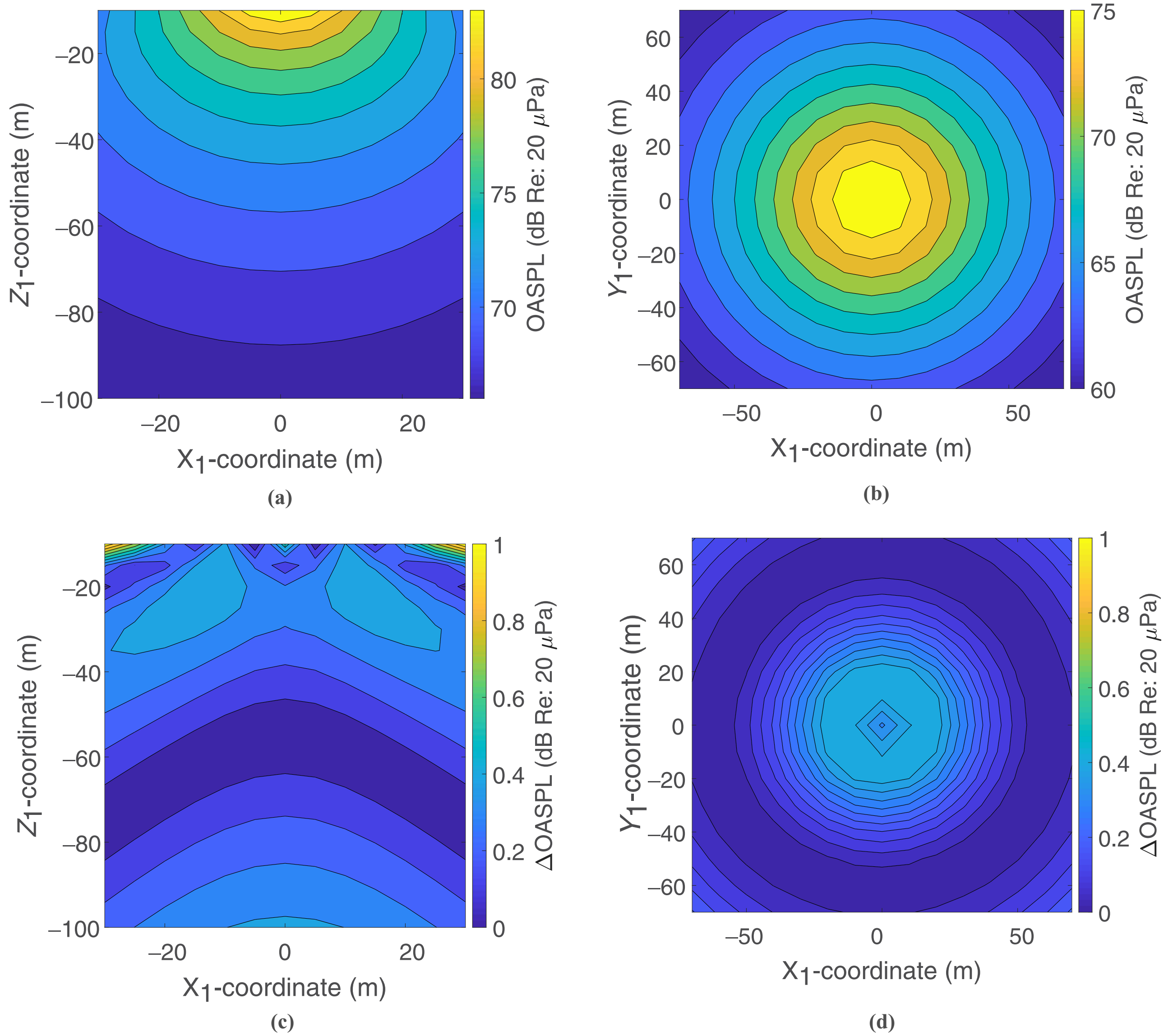

Fig. 14. OASPL calculated from rotor attenuation equation and its difference to UCD-QuietFly: (a) OASPL calculated by Eq. (13) on the X_1Z_1 plane, (b) OASPL calculated by Eq. (13) on the X_1Y_1 plane, (c) absolute difference between Fig. 14(a) and Fig. 13(a) on the X_1Z_1 plane, and (d) absolute difference between Fig. 14(b) and Fig. 13(b) on the X_1Y_1 plane.

constants as

$$\beta_1 = 0.0209; \qquad \beta_2 = 18.2429; \qquad \beta_3 = 6.7267 \tag{14}$$

It is worthwhile noting that it is possible to predict noise levels at the entire observer plane with only one noise level at a reference position and using Eqs. (13) and (14). Since the noise level at the reference location is used to propagate the sound to far-field observers, Eq. (13), along with Eq. (14), only accounts for sound propagation effects. In other words, Eqs. (13) and (14) are expected to work for any rotorcraft designs or operating conditions as long as the noise level at the reference location is provided.

Figure 14 shows the OASPL calculated by Eq. (13), where its average difference in comparison with the direct UCD-QuietFly predictions is 0.0147 dB, or 0.018% of the OASPL. Such a small difference demonstrates a good representation of the combination of rotor noise attenuation and directivity in the proposed semianalytic equation form. The differences between the UCD-QuietFly and Eq. (13) are presented in Figs. 14(c) and 14(d), demonstrating a close match except for small elevation angles. Comparing the computation time of about 1 min at a single observer location using UCD-QuietyFly with instant calculations of Eq. (13), the computational time saved using this approach is a factor of N, where N denotes the number of observers.

SPL predicted by Eq. (13) is compared with UCD-QuietFly results at multiple elevation angles and distances in Fig. 15. As expected, it is clearly shown that the OASPL decreases with increasing the distance and increases with increasing the elevation angle. It is shown that Eq. (13) accurately predicts the attenuation and directivity trends except for small elevation angle. Figure 15 also shows that at low elevation angles, the noise reduction is steeper with increasing the observer distance.

Conclusion

This paper presented a new computational approach to predict rotor trailing-edge noise considering helicopter rotor blades' full motions.

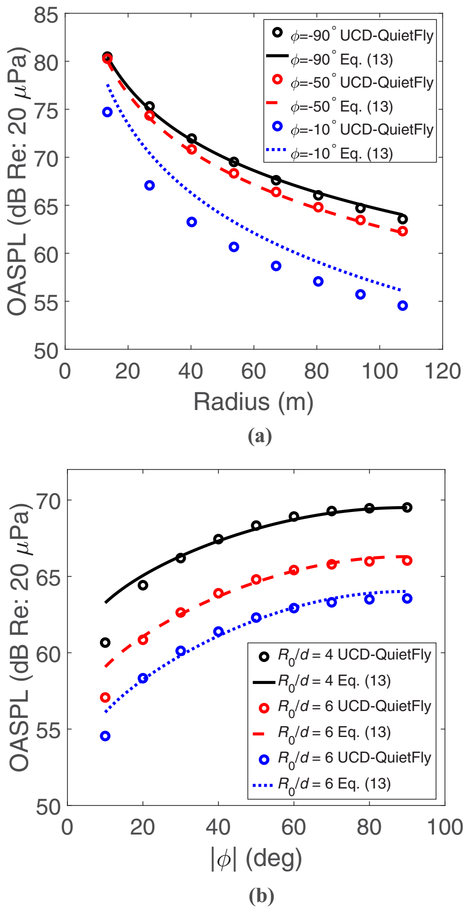

Fig. 15. Comparison of UCD-QuietFly and Eq. (13): (a) OASPL versus observer distance and (b) OASPL versus elevation angle.

The method combined the BEMT, XFOIL, Lee's empirical wall pressure spectrum model, and Amiet model to predict the local angle of attack, boundary-layer parameters, turbulence wall pressure spectrum, and trailing-edge noise. The numerical code, which is referred to as UCD-QuietFly, was validated against measurement data for airfoil noise and helicopter noise in hover. Key findings are summarized as follows:

1) Rotor trailing-edge noise is scaled with the 4.5th to fifth power of the tip Mach number for typical helicopter collective pitch and blade twist angles, and the frequency is scaled with $f * 0.8/M_{\text{tip}}$.

2) Although rotational speed still significantly affects the rotor trailing-edge noise, neglecting other parameters results in considerable inaccuracies. For example, an increased collective pitch angle increases the noise levels at low- to midfrequencies while maintaining high-frequency noise. The blade twist angle was observed to have a similar effect as the collective pitch angle. An increased rotor solidity only increases low- to midfrequency noise levels. An increased rotor radius with the constant tip Mach number results in higher noise for all frequencies mainly due to the increased source region. In addition, an increased ascending speed shows the negligible effect on rotor trailing-edge noise due to the operational limit of the helicopter maximum ascending speed. Increasing disk loading is found to decrease rotor trailing-edge noise for the entire frequency. Finally, for the increasing number of blades, low- to midfrequency noise is decreased while high-frequency noise is increased.

3) For a hovering helicopter, the vertical plane (X_1Y_1) has a dipole shape directivity pattern whereas the horizontal plane (X_1Y_1) has a circular monopole directivity pattern. A semianalytic equation was proposed to represent the geometric attenuation and directivity of rotor trailing-edge noise. This equation requires SPL at one reference observer location, which can be obtained by UCD-Quietfly or any other methods including measurement. It should be noted that this semianalytic equation is independent of helicopter designs or operation conditions since it only accounts for the attenuation and directivity of sound propagation. The effect of helicopter designs and operating conditions should be accounted for noise levels at the reference location. It was shown that this proposed equation provided good agreement with direct noise computations on the observer plane except shallow elevation angles. The computational time saving of an order of the number of observers can be achieved using this semianalytic equation.

4) Considering the high-frequency noise dominance, trailing-edge noise is important in terms of human perception, which should be accounted for rotorcraft blade design. In a preliminary rotorcraft design process, for example, UCD-QuietFly can be used to compare trailing-edge noise generated on various vehicle and blade designs. In addition, the design parameters can be optimized for trailing-edge noise by performing a parameter sweep in UCD-QuietFly.

5) More work is recommended to obtain the scaling of other parameters, beyond Mach number, on rotor trailing-edge noise, from which a rotor trailing-edge noise scaling law can be deduced.

Appendix

The expanded form of the directivity term D_ϕ is shown in Eq. (A1), which is obtained by performing the coordinate transformations in Eqs. (2) and (3).

$$\begin{aligned} D_\phi = {} & A_1 \cdot ((\sin(\theta_0+\theta)(r\cos\beta_p + Z_1\cos t - X_1\sin t) \\ & + \cos(\theta_0+\theta)\sin\phi\cdot A_2 - \cos(\theta_0+\theta)\cos\phi\cdot A_3)^2 \\ & + A_1 + (\cos\phi * A_2 + \sin\phi\cdot A_3)^2)^{-2} \end{aligned} \tag{A1}$$

where A_1, A_2, and A_3 in Eq. (A1) are shown as follows for clarity:

$$\begin{aligned} A_1 = {} & (\cos(\theta_0+\theta)(r\cos\beta_p + Z_1\cos t - X_1\sin t) \\ & - \sin(\theta_0+\theta)\sin\phi\cdot A_2 + \sin(\theta_0+\theta)\cos\phi\cdot A_3)^2 \end{aligned} \tag{A2}$$

$$A_2 = X_1\cos t + Z_1\sin t - r\cos\phi\sin\beta_p \tag{A3}$$

$$A_3 = Y_1 - r\sin(\beta_p)\sin(\phi) \tag{A4}$$

The conversion from the narrow-band sound pressure level (SPL) to one-third octave band sound pressure level ($\text{SPL}_{1/3}$) is provided in Eq. (A5), where f_n is the midband frequency, $m_{l,n}$ and $m_{u,n}$ are the lower and upper bounds frequency indices of the nth band, and $\text{SPL}_{\text{rotor},i}$ is the narrow-band SPL in Eq. (10) that is interpolated into 1-Hz intervals.

$$\text{SPL}_{1/3,n} = 10\log_{10}\left(\int_{f_{l,n}}^{f_{u,n}} \frac{2\pi S_{\text{pp}}}{(2\times 10^{-5})^2} df\right) = 10\log_{10}\sum_{i=m_{l,n}}^{m_{u,n}} 10^{0.1\text{SPL}_{\text{rotor},i}} \tag{A5}$$

$$f_n = 1000\times 2^{(n-30)/30};\quad f_{l,n} = f_n/2^{1/6};\quad f_{u,n} = f_n\times 2^{1/6} \tag{A6}$$

The conversion from the narrow-band SPL to (OASPL is provided in Eq. (A7). In this paper, the OASPL is integrated from the SPL in the frequency range of $f_0 = 0.1$ kHz to $f_1 = 10$ kHz. Before computing OASPL and $\text{SPL}_{1/3}$, narrow-band SPL is interpolated into 1-Hz intervals:

$$\text{OASPL} = 10\log_{10}\left(\int_{f_0}^{f_1} \frac{2\pi S_{\text{pp}}}{(2\times 10^{-5})^2} df\right) = 10\log_{10}\sum_{i=1}^{n_f} 10^{0.1\text{SPL}_{\text{rotor},i}} \tag{A7}$$

where n_f is the number of 1-Hz frequency intervals from f_0 to f_1.

Acknowledgments

This research was funded by Hyundai Motor Company for a project of urban air mobility aircraft broadband noise prediction.

References

[1]Snider, R., Samuels, T., Goldman, B., and Brentner, K., "Full-Scale Rotorcraft Broadband Noise Prediction and Its Relevance to Civil Noise Certification Criteria," Proceedings of the 69th Annual Forum of the American Helicopter Society, Phoenix, AZ, May 21–23, 2013.

[2]Intaratep, N., Alexander, W, and Devenport, W., "Experimental Study of Quadcopter Acoustics and Performance at Static Thrust Conditions," AIAA 2016-2873, Proceedings of the 22nd AIAA/CEAS Aeroacoustics Conference, Lyon, France, May 30–June 1, 2016.

[3]Zawodny, N., Boyd, D., and Burley, C., "Acoustic Characterization and Prediction of Representative, Small-Scale Rotary-Wing Unmanned Aircraft System Components," Proceedings of the 72nd Annual Forum of the American Helicopter Society, West Palm Beach, FL, May 17–19, 2016.

[4]Zawodny, N., and Boyd, D., "Investigation of Rotor-Airframe Interaction Noise Associated with Small-Scale Rotary-Wing Unmanned Aircraft Systems," *Journal of the American Helicopter Society*, Vol. 65, (1), 2020, pp. 1–17.

[5]Brooks, T. F., Pope, D. S., and Marcolini, M. A., "Airfoil Self-Noise and Prediction," NASA RP 1218, 1989.

[6]Ffowcs Williams, J. E., and Hall, L., "Aerodynamic Sound Generation by Turbulent Flow in the Vicinity of a Scattering Half Plane," *Journal of Fluid Mechanics*, Vol. 40, (4), 1970, pp. 657–670.

[7]Lighthill, M., "On Sound Generated Aerodynamically I. General Theory," *Proceedings of the Royal Society*, Vol. A211, 1952, pp. 564–587.

[8]Curle, N., "The Influence of Solid Boundaries upon Aerodynamic Sound," *Proceedings of the Royal Society*, Vol. A231, 1955, pp. 505–514.

[9]Amiet, R., "Noise Due to Turbulent Flow Past a Trailing Edge," *Journal of Sound and Vibration*, Vol. 47, (3), 1976, pp. 387–393.

[10]Schlinker, R. H., and Amiet, R. K., "Helicopter Rotor Trailing Edge Noise," NASA RP 3470, 1981.

[11]Kim, Y. N., and George, A. R., "Trailing-Edge Noise from Hovering Rotors," *AIAA Journal*, Vol. 20, (9), 1982, pp. 1167–1174.

[12]Ffowcs Williams, J. E., and Hawkings, D. L., "Theory Relating to the Noise of Rotating Machinery," *Journal of Fluid Mechanics*, Vol. 10, (1), 1969, pp. 10–21.

[13]Blandeau, V., and Joseph, P., "Validity of Amiet's Model for Propeller Trailing-Edge Noise," *AIAA Journal*, Vol. 49, (5), 2011, pp. 1057–1066.

[14]Goody, M., "Empirical Spectral Model of Surface Pressure Fluctuations," *AIAA Journal*, Vol. 42, (9), 2004, pp. 1788–1794.

[15]Burley, C. L., and Brooks, T. F., "Rotor Broadband Noise Prediction with Comparison to Model Data," *Journal of the American Helicopter Society*, Vol. 49, (1), 2004, pp. 28–42.

[16]Lee, S., "Empirical Wall-Pressure Spectral Modeling for Zero and Adverse Pressure Gradient Flows," *AIAA Journal*, Vol. 56, (5), 2018, pp. 1818–1829.

[17]Hutcheson, F. V., and Brooks, T. F., "Effects of Angle of Attack and Velocity on Trailing Edge Noise," Proceedings of the 42nd AIAA Aerospace Sciences Meeting and Exhibit, Reno, NV, January 5–8, 2004.

[18]Lee, S., "The Effect of Airfoil Shape on Trailing Edge Noise," *Journal of Theoretical and Computational Acoustics*, **27**, 1850020 (2019).

[19]Chou, S.-T., and George, A.R., "Effect of Angle of Attack on Rotor Trailing-Edge Noise," *AIAA Journal*, Vol. 22, (12), 1984, pp. 1821–1823.

[20]Drela, M., "XFOIL: An Analysis and Design System for Low Reynolds Number Airfoils," edited by T. J. Mueller, *Low Reynolds Number Aerodynamics*, Lecture Notes in Engineering, Vol. 54, Springer, Berlin, Germany, 1989, pp. 1–12.

[21]Herr, M., Ewert, R., Rautmann, C., Kamruzzaman, M., Bekiropoulos, D., Iob, A., Arina, R., Batten, P., Chakravarthy, S., and Bertagnolio, F., "Broadband Trailing-Edge Noise Predictions—Overview of BANC-III Results," Proceedings of the 21st AIAA/CEAS Aeroacoustics Conference, Dallas, TX, June 22–26, 2015.

[22]Lee, S., and Shum, J., "Prediction of Airfoil Trailing-Edge Noise Using Empirical Wall-Pressure Spectrum Models," *AIAA Journal*, Vol. 57, (3), 2019, pp. 888–897.

[23]Johnson, H. K., and Katz, W. M., "Investigation of the Vortex Noise Produced by a Helicopter Rotor," USAAMRDL RP 72-2, 1972.

[24]Leverton, J. W., "The Noise Characteristics of a Large 'Clean' Rotor," *Journal of Sound and Vibration*, Vol. 27, (3), 1973, pp. 357–376.

[25]Brentner, K. S., Zolbayar, B., and Jaworski, T. F., "An Investigation of Noise from Electric, Low-Tip-Speed Aircraft Propellers," Proceedings of the AHS International Technical Meeting on Aeromechanics Design for Transformative Vertical Flight 2018, San Francisco, CA, January 16–18, 2018.

[26]Floros, M. W., "Performance and Acoustics of Small Rotors with Non-Uniform Blade Spacing," Proceedings of the Vertical Flight Society 75th Annual Forum & Technology Display, Philadelphia, PA, May 13–16, 2019.

[27]International Organization for Standardization, "Acoustics—Attenuation of Sound During Propagation Outdoors," ISO 9613-2, 1996.